The Astrophysical Journal Letters, 855:L26 (6pp), 2018 March 10 https://doi.org/10.3847/2041-8213/aab3dc

2004 EW_{95}: A Phyllosilicate-bearing Carbonaceous Asteroid in the Kuiper Belt

Tom Seccull[1], Wesley C. Fraser[1], Thomas H. Puzia[2], Michael E. Brown[3], and Frederik Schönebeck[4]
[1] Astrophysics Research Centre, Queen's University Belfast, Belfast BT7 1NN, UK; tseccull01@qub.ac.uk
[2] Institute of Astrophysics, Pontificia Universidad Católica de Chile, Av. Vincuña Mackenna 4860, 7820436, Santiago, Chile
[3] Division of Geological and Planetary Sciences, California Institute of Technology, Pasadena, CA 91125, USA
[4] Astronomisches Rechen-Institut, Zentrum für Astronomie der Universität Heidelberg, Mönchhofstraße 12-14, D-69120 Heidelberg, Germany
Received 2018 January 29; revised 2018 March 2; accepted 2018 March 3; published 2018 March 15

Abstract

Models of the Solar System's dynamical evolution predict the dispersal of primitive planetesimals from their formative regions among the gas-giant planets due to the early phases of planetary migration. Consequently, carbonaceous objects were scattered both into the outer asteroid belt and out to the Kuiper Belt. These models predict that the Kuiper Belt should contain a small fraction of objects with carbonaceous surfaces, though to date, all reported visible reflectance spectra of small Kuiper Belt Objects (KBOs) are linear and featureless. We report the unusual reflectance spectrum of a small KBO, (120216) 2004 EW_{95}, exhibiting a large drop in its near-UV reflectance and a broad shallow optical absorption feature centered at ~700 nm, which is detected at greater than 4σ significance. These features, confirmed through multiple epochs of spectral photometry and spectroscopy, have respectively been associated with ferric oxides and phyllosilicates. The spectrum bears striking resemblance to those of some C-type asteroids, suggesting that 2004 EW_{95} may share a common origin with those objects. 2004 EW_{95} orbits the Sun in a stable mean motion resonance with Neptune, at relatively high eccentricity and inclination, suggesting it may have been emplaced there by some past dynamical instability. These results appear consistent with the aforementioned model predictions and are the first to show a reliably confirmed detection of silicate material on a small KBO.

Key words: Kuiper belt objects: individual (2004 EW95) – minor planets, asteroids: general – techniques: photometric – techniques: spectroscopic

1. Introduction

Current models of the Solar System's dynamical evolution, such as the Nice model (Gomes et al. 2005; Morbidelli et al. 2005; Tsiganis et al. 2005; Levison et al. 2011), predict that the Kuiper Belt should largely be composed of objects that formed beyond the giant planet region. Concurrently, the Grand Tack model (Walsh et al. 2011, 2012) posits that the primitive carbonaceous asteroids formed among the giant planets and were injected into the outer asteroid belt due to the early migrations of Jupiter and Saturn. By the same mechanism the Grand Tack model also predicts that carbonaceous asteroids could have been scattered outward into the Kuiper Belt region, suggesting that a small number of objects beyond Neptune would possess primitive, dark, carbon-rich, asteroidal surfaces like those of C/D/P-type asteroids.

The optical ($400 \leqslant \lambda \leqslant 900$ nm) reflectance spectra of small Kuiper Belt Objects (KBOs) typically exhibit a red, linear, featureless slope that reveals little about their surface composition (Fornasier et al. 2009). So far the only material commonly found on the surfaces of small KBOs is water ice, which characteristically absorbs in the near infrared (NIR) at ~1.5 μm and ~2.0 μm (Barucci et al. 2011; Brown et al. 2012). No diagnostic optical features have been confirmed.

(120216) 2004 EW_{95} is a small 3:2 resonant KBO with absolute magnitude $H_R = 6.31 \pm 0.05$ (Peixinho et al. 2015) and radiometric diameter $r = 291.1^{+20.3}_{-25.9}$ km (Mommert et al. 2012). Its reflectance spectrum was initially revealed to be atypical of KBO spectra from optical and NIR spectral photometry gathered with the *Hubble Space Telescope* (*HST*; Fraser et al. 2015). Of the eight small outer Solar System objects observed in *HST* GO-Program 12234, 2004 EW_{95} was unique in that instead of exhibiting a linear optical spectrum, it possessed an apparent upward curvature through the optical range. This peculiar property of the object, along with hints of a drop in its near-UV reflectance (Fraser et al. 2015), warranted subsequent spectroscopic observations.

2. Observations

We observed 2004 EW_{95} twice at the European Southern Observatory's (ESO's) Very Large Telescope (VLT), during 2014 August 3 and 2017 April 22–23 using the X-Shooter (Vernet et al. 2011) and FORS2 (Appenzeller et al. 1998) spectrographs, respectively.

X-Shooter is a medium-resolution echelle spectrograph with three arms covering the near-UV/blue (UVB; 300–560 nm), visual (VIS; 550–1020 nm), and NIR (1024–2480 nm) spectral range. While 2004 EW_{95} was observed in all three of X-Shooter's arms simultaneously, the NIR observations had such a low signal-to-noise ratio (S/N) that they could not be properly reduced. Hence, from this point we only consider the UVB and VIS observations. The UVB and VIS detectors share a common pixel scale of $0\farcs16$ and slit length of $11''$. We set the UVB and VIS slits to widths of $1\farcs0$ and $0\farcs9$, each providing a respective resolving power of ~5100 and ~8800. All observations were performed with a UVB and VIS detector readout binning of 1×2, except for observations of the solar calibrator HD 117286, when no binning was performed. The difference in binning between 2004 EW_{95} and HD 117286 produces no observable change to the features we detect in the UVB and VIS reflectance spectrum when compared to those calibrated with the other stars.

The X-Shooter observations were performed in a three-point dither pattern to mitigate bad pixel artifacts and contamination

Table 1
Spectroscopy Observation Details

Target	Observation Date | UT Time	Exposure Time (s)			Airmass	Seeing (″)
FORS2 Night 1						
BD-00 2514	2017 Apr 22 | 01:30:52–01:41:46	12.0			1.126–1.127	0.51–0.51
TYC-4949-897-1	2017 Apr 22 | 02:43:21–02:50:52	12.0			1.106–1.107	0.57–0.59
HD 106436	2017 Apr 22 | 02:57:45–03:07:26	6.0			1.005–1.005	0.67–0.69
HD 106649	2017 Apr 22 | 03:07:30–03:13:23	3.0			1.003–1.003	0.56–0.56
2004 EW95	2017 Apr 22 | 03:26:06–04:10:18	500.0			1.039–1.092	0.54–0.66
HD 136122	2017 Apr 22 | 04:10:54–04:19:18	3.0			1.087–1.087	0.54–0.59
HD 140854	2017 Apr 22 | 04:19:24–04:27:41	3.0			1.125–1.125	0.58–0.58
FORS2 Night 2						
HD 106436	2017 Apr 23 | 02:13:57–02:21:40	6.0			1.012–1.012	0.65–0.68
HD 106649	2017 Apr 23 | 02:22:15–02:30:42	3.0			1.005–1.005	0.57–0.57
2004 EW95	2017 Apr 23 | 02:37:58–03:27:35	500.0			1.116–1.183	0.60–0.72
HD 136122	2017 Apr 23 | 03:36:06–03:46:12	3.0			1.149–1.149	0.71–0.72
HD 140854	2017 Apr 23 | 03:46:22–03:49:38	3.0			1.203–1.206	0.62–0.69
X-Shooter		UVB	VIS	NIR		
HD 117286	2014 Aug 02 | 23:42:36–23:48:40	3.0	3.0	3.0	1.170–1.188	1.25–1.60
2004 EW95	2014 Aug 03 | 00:21:15–01:55:31	500.0	466.0	532.0	1.166–1.715	0.99–1.30
HIP 077439	2014 Aug 03 | 02:08:38–02:12:04	3.0	3.0	3.0	1.331–1.347	1.33–1.67
HIP 075235	2014 Aug 03 | 02:19:27–02:23:05	3.0	3.0	3.0	1.568–1.579	1.19–1.69

Note. Stars used to calibrate the spectra in Figures 2 and 3 are highlighted in bold.

by cosmic rays in the stacked spectrum. The slit was realigned to the parallactic angle at the beginning of each observation to reduce the effects of atmospheric differential refraction; this was especially important in light of X-Shooter's disabled Atmospheric Dispersion Corrector (ADC) at the time of observing. Of nine total observed exposures of 2004 EW_{95}, seven were usable. Two exposures where the object appeared to drift off the slit were ignored during data reduction. Three solar calibrator stars, HD 117286, Hip 075235, and Hip 077439, were similarly observed adjacent in time to 2004 EW_{95} and at similar airmass. Flux calibrators EG 274 and Feige 110 were observed as part of the standard calibration program. Details of observing conditions are reported in Table 1.

FORS2 is a multipurpose spectrograph and imager. We obtained FORS2 spectra of 2004 EW_{95} over two nights in Long Slit Spectroscopy mode with a two-point dither pattern, using the blue sensitive E2V detector, the standard resolution collimator, and the 600B+22 grism. At the beginning of each image pair the slit was realigned to the parallactic angle. On each night four exposures were obtained for 2004 EW_{95}. In addition, on each night two solar calibrators were observed just before and just after 2004 EW_{95}. These calibrators were: HD 106436, HD 106649, HD 136122, and HD 140854. Two additional solar calibrators (BD-00 2514 and TYC-49494-897-1) were observed two hours prior to 2004 EW_{95} on night one. All of the solar calibrators were observed at similar airmass to 2004 EW_{95}. BD-00 2514, the star that produced the lowest calibration residuals below 400 nm and at 517 nm, was used to calibrate the science spectra presented in Section 4. Flux standards were observed, but the images were later found to be saturated and therefore useless. During the reduction process all of the FORS2 spectra were corrected for airmass extinction using the instrument extinction table. Over both nights the cloud cover never warranted greater than a "Clear" designation and does not appear to have affected the slope of the final spectra. Further details on the FORS2 observations are reported in Table 1.

3. Data Reduction

Standard reduction steps (including order rectification and merging, and flux calibration in the case of X-Shooter) were performed for all of the observed spectra with the ESO-provided instrument pipelines (X-Shooter v.2.7.1; FORS2 v.5.3.2, Modigliani et al. 2017; Smoker et al. 2017) in the ESO Reflex data processing environment (v. 2.8.4 and v. 2.8.5, respectively; Freudling et al. 2013).

We applied two different methods for sky subtraction, cosmic-ray removal, and extraction of the spectra. This was done to test the consistency of the two methods and confirm that any observed features were not simply reduction artifacts.

3.1. Method 1

Due to X-Shooter's disabled ADC at the time we observed 2004 EW_{95}, the spectra were found to have a wavelength-dependent spatial position in the 2D rectified images, which was most pronounced at the shortest wavelengths (see Figure 1). The point spread function (PSF) of the spectrum was also wavelength dependent, due to a combination of variations across X-Shooter's echelle orders and wavelength-dependent seeing. These factors made a simple straight extraction of the 1D spectrum impossible without including increased background noise in the extracted spectrum. A Python script was created to track the wavelength-dependent spectrum width and center within each image to evaluate wavelength-dependent extraction limits, thus preserving S/N while avoiding wavelength-dependent extraction losses, especially in the near-UV. The script worked as follows.

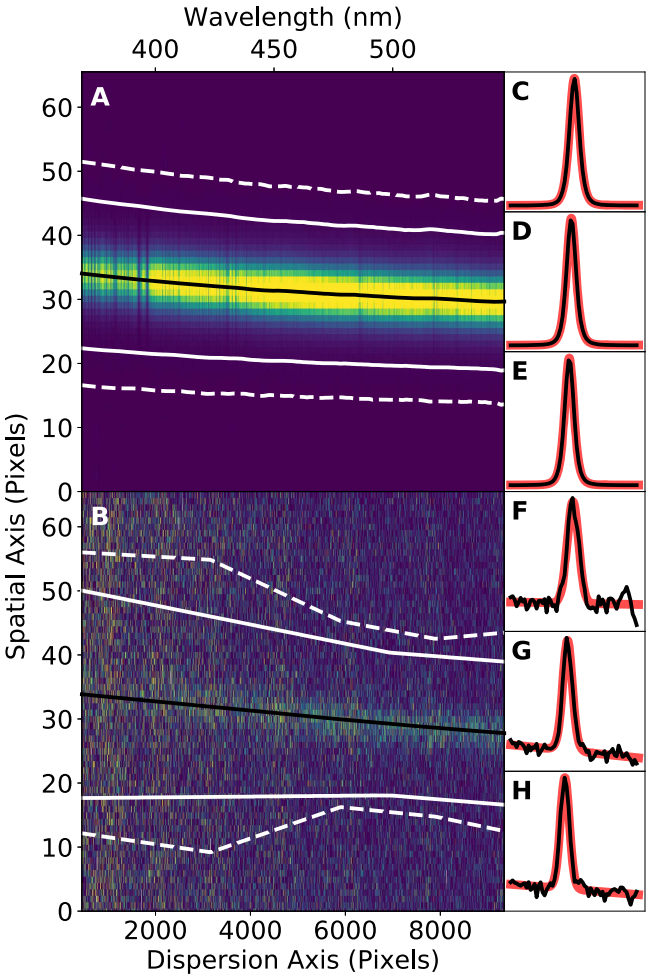

Figure 1. Diagram of the method 1 reduction process for the 2D flux calibrated, rectified, and merged UVB X-Shooter spectra of solar calibrator star HD 117286 (panels (A), (C)–(E)) and 2004 EW_{95} (panels (B), (F)–(H)). The amount of flux gathered for HD 117286 in panel (A) is ∼5 orders of magnitude greater than that gathered for 2004 EW_{95} in panel (B). Panels (A) and (B) show lines tracing the sky subtraction limits (dashed white) used to subtract the sky flux from these images. Also shown are lines tracing the Moffat profile centers for each extraction bin along the dispersion axis (solid black), and their associated extraction limits (solid white). Panels (C)–(H) show the median spatial profiles of example data bins taken from various wavelengths along the spectrum (black), fitted with their associated Moffat profiles (red).

To first remove the highly variable background level, each 2D pipeline reduced and flux-calibrated spectrum was binned along the dispersion axis. The bins were progressively widened until the S/N of the summed spatial profile reached a predetermined threshold. Moffat profiles (Moffat 1969) were fitted to the median spatial profile of each bin in order to define the science extraction limits and sky regions. Sky region boundaries were taken as the pixels outside ±3 FWHM from each Moffat profile center. These boundaries were then linearly interpolated across the full unbinned image. In each unbinned wavelength element the background value was taken as the median value in the sky regions and was subtracted from the image at that wavelength. Cosmic rays in the sky regions and target regions were then separately sigma clipped at 5σ. The binning and fitting process was repeated on the background subtracted images to define the target extraction limits on the sky subtracted image. The science extraction limits were set to ±2 FWHM from each Moffat profile center (see Figure 1). The flux within the interpolated extraction limits was summed for each unbinned wavelength element to extract the 1D spectrum. Dithers in which the FWHM extraction boundaries fell off the image were omitted from later stacking.

3.2. Method 2

The spectra were reduced using only the ESO Reflex instrument pipelines (Freudling et al. 2013) which performed the sky subtraction, cosmic-ray flagging, and spectrum extraction as described in the pipeline user manuals (Modigliani et al. 2017; Smoker et al. 2017). The FORS2 spectra were extracted with both optimal (Horne 1986) and aperture methods, while the X-Shooter spectra were extracted with only the aperture method. The widths of the straight extraction apertures for each spectrum were set at the greatest separation between the extraction limits calculated using method 1.

All methods tested produced spectra with consistent features for both FORS2 and X-Shooter observations. However, spectra extracted via method 1 showed increased S/N relative to those reduced via method 2. For this reason the spectra presented in Section 4 were extracted via method 1.

Following extraction, the individual spectra were normalized, median stacked, solar calibrated, and binned. Dithers with extremely low S/N were omitted from the final stack. Regions near ∼456, ∼560, and ∼640 nm in the X-Shooter spectrum were rejected to avoid copious artifacts produced by bad pixels and the edges of the echelle orders.

Because the UVB arm and VIS arm of the X-Shooter spectrum were normalized at different wavelengths during stacking, the arms required rescaling relative to each other to produce a continuous spectrum. The scaling factor of UVB relative to VIS was calculated as the ratio between the relative flux of the KBO with respect to the flux of the solar calibrator star measured at the wavelengths of normalization in each arm. The scaling was then adjusted to account for the spectral slope in the region where the UVB and VIS arms join.

In all spectra the shortest wavelength has been limited to ∼400 nm due to large residuals produced by differences in metallicity and temperature between the solar calibrators used and the Sun (Hardorp 1980).

The FORS2 spectrum presented in Figures 2 and 3 comprises observations only from night 1, observed under photometric conditions.

To further display the integrity of our reduction methods we show the spectrum of the KBO 1999 OX_3 in Figure 3. The X-Shooter data of this target exhibit a very similar S/N as in the X-Shooter data of 2004 EW_{95}. Thus, any extraction issues of our pipeline that may be apparent in the spectra of 2004 EW_{95} should be equally apparent in the spectra of 1999 OX_3. As can be seen in Figure 3, the spectra produced with extraction method 1 result in a typical KBO spectrum; that is linear, featureless, red, and exhibits no identifiable absorption features. Hence, we conclude that the features observed in the spectrum of 2004 EW_{95} are not reduction artifacts and instead are inherent to the spectrum itself. Via linear regression, the optical slope of 1999 OX_3's spectrum was measured to be $30.6 \pm 1.5\%$ per 100 nm, in accord with literature values (Peixinho et al. 2015).

4. Results and Discussion

We have detected two features in the reflectance spectrum of 3:2 resonant KBO 2004 EW_{95}: a large drop in reflectance at

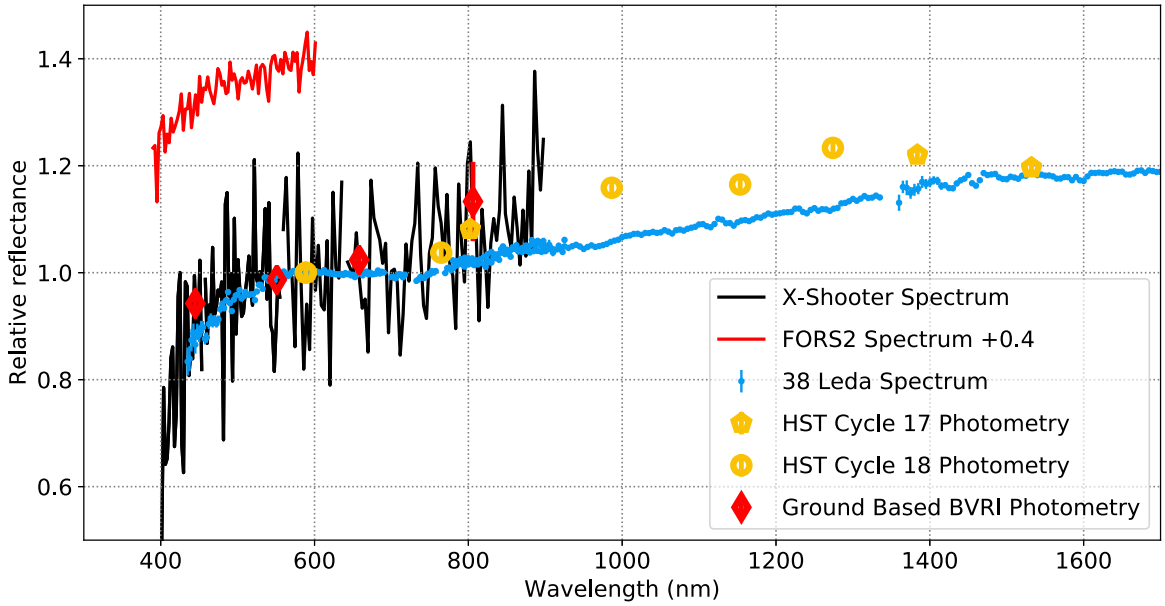

Figure 2. Reflectance spectra and photometry (Fraser et al. 2015) of 2004 EW_{95} compared to the combined optical and NIR reflectance spectrum of the hydrated C-type asteroid, 38 Leda from the SMASSII and SMASSir catalogs (Bus & Binzel 2002a, 2002b; DeMeo et al. 2009). 2004 EW_{95}'s drop in reflectance toward the UV is clearly visible in both the X-Shooter and FORS2 spectra, matching well with 38 Leda. The presence of the broad feature centered near 700 nm is apparent in both the X-Shooter spectrum and the *HST* spectrophotometry. We attribute this feature to phyllosilicate absorption like that of the hydrated C-type asteroids. The NIR behavior observed for 2004 EW_{95} in the *HST* photometry closely resembles the NIR spectral behavior of C-type asteroids, presenting a featureless red slope, remaining roughly constant from ∼1000 nm to ∼1400 nm. 2004 EW_{95}'s reflectance drops slightly at ∼1500 nm, hinting at possible absorption due to surface water ice. Reflectances in all data sets are normalized at 589 nm. The FORS2 spectrum (in red) is offset by +0.4 for clarity. The apparent difference in overall slope between overlapping regions of the FORS2 and X-Shooter spectra are calibration artifacts resulting from the use of slightly different solar analog stars.

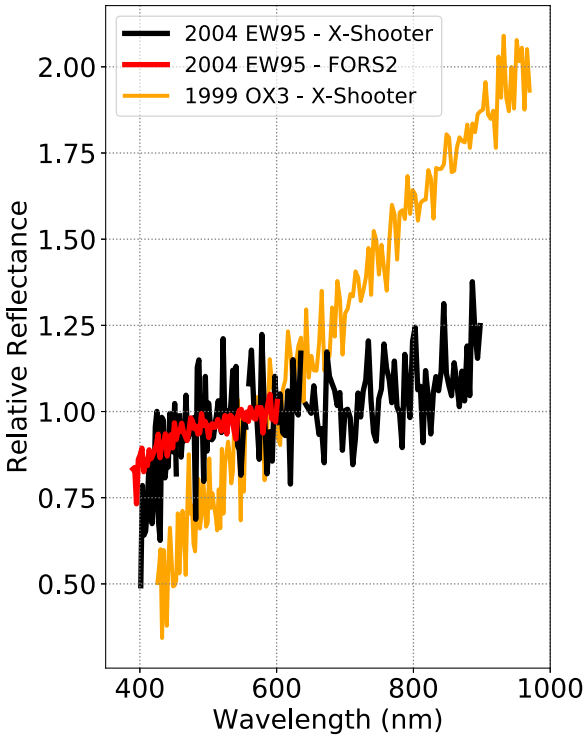

Figure 3. Spectrum comparison plot. Here we compare the spectra of 2004 EW_{95} observed with X-Shooter and FORS2, along with the X-Shooter spectrum of a typical KBO, 1999 OX_3. Both spectra of 2004 EW_{95} agree with each other very well at wavelengths greater than ∼430 nm. Below ∼430 nm there is a divergence in the slope of each spectrum caused by difference in color of the solar calibrators used. Both 2004 EW_{95} and 1999 OX_3 were of similar brightness when observed. All spectra have been reduced using the method 1 extraction technique described in Section 3.

wavelengths below 550 nm, and a broad (∼0.2–0.3 μm wide), shallow absorption feature centered at around 700 nm (see Figure 2). Previously, neither feature has ever been reliably detected in the spectrum of a KBO. Each of these two features has been independently observed by two separate instruments, and are present in the reported reflectance spectra regardless of which of our solar calibrator targets, or which of two separate spectral extraction techniques, were used in our data reduction.

The FORS2 and X-Shooter spectra of 2004 EW_{95} fully agree above 430 nm (see Figure 3). At 415 nm the X-Shooter spectrum has a greater spectral slope and is discrepant from the FORS2 spectrum in that wavelength range by $\sim 2\sigma$. This difference corresponds to the known difference in $B-V$ color between the solar calibrator stars used to calibrate each spectrum.

The UV-optical spectrum of 2004 EW_{95} bears a striking resemblance to those of primitive carbonaceous asteroids. Specifically, 2004 EW_{95} resembles a hydrated C-type asteroid (Bus & Binzel 2002b; DeMeo et al. 2009; Vernazza et al. 2016; we compare 2004 EW_{95} to the asteroid 38 Leda in Figure 2). The shallow optical absorption feature at ∼700 nm defines the hydrated Ch/Cgh asteroid subclasses, being observed in ∼30% of C-types (Rivkin 2012), and has been associated with charge transfer in aqueously altered silicate material (Vilas & Gaffey 1989; Fornasier et al. 2014; Rivkin et al. 2015). To characterize the ∼700 nm feature and test the significance of its detection, we first remove a linear continuum slope of 3.6% per 100 nm that was determined from a linear fit to the 530–580 nm and 850–900 nm wavelength ranges. A Gaussian profile was then fit to the continuum in a maximum likelihood sense, using the emcee Monte Carlo Markov Chain sampler (Foreman-Mackey et al. 2013). We adopt as a best fit the

median sample point, uncertainty as the 1σ sampling range when marginalizing over the other parameters. The best-fit depth, center, and FWHM were 4^{+1}_{-1}%, 734^{+43}_{-45} nm and 319^{+101}_{-101} nm, respectively. The 4σ lower limit on the feature depth is 1% demonstrating the veracity of the detection. Technically, our routine quoted a higher significance of detection; however, at this high a significance, the ability to determine the continuum is the ultimate limiting factor.

Indications for phyllosilicate features have previously been reported in the spectra of KBOs 2003 AZ_{84} (Fornasier et al. 2004), 2000 EB_{173} (38628 Huya) and 2000 GN_{171} (Lazzarin et al. 2003; de Bergh et al. 2004). Follow-up spectra of sufficient quality to detect those reported features, however, have revealed featureless spectra on later occasions, with rotational spectral variability reported as a possible but unconfirmed explanation for the disappearance of the feature on these objects (Fornasier et al. 2004, 2009; Merlin et al. 2017). Repeat photometric observations of 2004 EW_{95} with *HST* reported by Fraser et al. (2015) have shown its spectrum to be invariable, which is supported by the consistency between that *HST* spectrophotometry of 2004 EW_{95} and the reflectance spectra reported in this work (see Figure 2). With multiple independent photometric and spectroscopic detections of the 700 nm feature in the spectrum of 2004 EW_{95} over multiple epochs, we report the first confident detection of phyllosilicates on any KBO.

Like 2004 EW_{95}, some S-, V-, and C-type asteroids also exhibit a drop in near-UV reflectance, including the hydrated C-types to which this spectrum is most similar. On asteroids the UV drop has been attributed to the presence of ferric oxide material (Bus & Binzel 2002a). It should be noted that other materials such as complex aromatic organics can also produce a similar drop-off (Izawa et al. 2014; Hendrix et al. 2016), though organic-rich bodies such as the P- and D-type asteroids have not been observed to exhibit this UV drop in their reflectance spectra (Bus & Binzel 2002a, 2002b; DeMeo et al. 2009; Marsset et al. 2014). Moreover, other than 2004 EW_{95} of the 41 published optical spectra of KBOs and centaurs with sufficient short wavelength coverage, only the centaur (32532) Thereus hints at the presence of a similar UV drop (Barucci et al. 2002), though the presence of this feature on Thereus has not yet been confirmed.

The longest wavelength at which 2004 EW_{95} was observed was in the *HST*/WFC3 153M filter centered at 1532.2 nm (see Figure 2). Here the observed reflectance of the object appears to decrease relative to the NIR photometric points from 1000–1400 nm. The decrease is consistent with the presence of a small amount of water ice, which characteristically absorbs at these wavelengths (Brown et al. 2012; Fraser & Brown 2012). This feature is the only one to distinguish the spectrum of 2004 EW_{95} from that of a C-type asteroid, and suggests that unlike the C-types in the outer asteroid belt, 2004 EW_{95} has retained its primordial surface water content.

The Grand Tack model (Walsh et al. 2011, 2012) predicts that as a result of the early migrations of Jupiter and Saturn, the primitive small bodies that formed between the gas giants would be scattered and injected into the outer asteroid belt, making up the bulk of the organic-rich asteroids. Models of Jupiter's and Saturn's rapid gas accretion show that primitive interplanetary asteroids could also be scattered as the gas giants formed (Raymond & Izidoro 2017). By either mechanism (they are not mutually exclusive), a small fraction of those bodies would be scattered outward into the Trans-Neptunian belt, where they could later be captured in the mean motion resonances (MMRs) of Neptune (Levison et al. 2008). 2004 EW_{95} orbits the Sun in Neptune's 3:2 MMR, at relatively high orbital eccentricity and inclination ($a = 39.316$ au, $e = 0.3139$, $i = 29.^{\circ}3$, Peixinho et al. 2015). The presence of a phyllosilicate feature indicates that 2004 EW_{95} has been subjected to significant heating, either radiogenic (McAdam et al. 2015), from a very large single collision or extensive collisional bombardment (Rubin 1995; McKinnon 2002), or via solar irradiation. The striking similarity between 2004 EW_{95} and certain C-type asteroids points to the plausible idea that 2004 EW_{95} shares a common origin with these objects. Taken together, the spectroscopic similarity to C-type asteroids and the orbital properties of 2004 EW_{95} are consistent with the idea that this object may have formed near Jupiter among the primordial C-type asteroids (Walsh et al. 2011) and was subsequently emplaced into the Kuiper Belt by the migrating planets.

We thank Faith Vilas and Alan Fitzsimmons for their encouraging constructive discussion and comments. This work is based on observations collected at the European Organisation for Astronomical Research in the Southern Hemisphere under ESO programs 093.C-0259(A), 095.C-0521(A) and 099.C-0651(A). W.C.F. acknowledges support from STFC grant ST/P0003094/1. T.H.P. acknowledges support through the FONDECYT Regular project No. 1161817 and the BASAL Center for Astrophysics and Associated Technologies (PFB-06). M.E.B. acknowledges support from the NASA Planetary Astronomy Program through grant NNX09AB49G.

Facility: ESO VLT(X-Shooter and FORS2).

Software: Astropy (The Astropy Collaboration et al. 2013) corner (Foreman-Mackey 2016) emcee (Foreman-Mackey et al. 2013) ESO Reflex (Freudling et al. 2013) matplotlib (Hunter 2007) numpy (van der Walt et al. 2011) scipy (Jones et al. 2001).

ORCID iDs

Tom Seccull https://orcid.org/0000-0001-5605-1702
Wesley C. Fraser https://orcid.org/0000-0001-6680-6558
Thomas H. Puzia https://orcid.org/0000-0003-0350-7061
Michael E. Brown https://orcid.org/0000-0002-8255-0545

References

Appenzeller, I., Fricke, K., Fürtig, W., et al. 1998, Msngr, 94, 1
Barucci, M. A., Alvarez-Candal, A., Merlin, F., et al. 2011, Icar, 214, 297
Barucci, M. A., Boehnhardt, H., Dotto, E., et al. 2002, A&A, 392, 335
Brown, M. E., Schaller, E. L., & Fraser, W. C. 2012, AJ, 143, 146
Bus, S. J., & Binzel, R. P. 2002a, Icar, 158, 106
Bus, S. J., & Binzel, R. P. 2002b, Icar, 158, 146
de Bergh, C., Boehnhardt, H., Barucci, M. A., et al. 2004, A&A, 416, 791
DeMeo, F. E., Binzel, R. P., Slivan, S. M., & Bus, S. J. 2009, Icar, 202, 160
Foreman-Mackey, D. 2016, JOSS, 1, 24
Foreman-Mackey, D., Hogg, D. W., Lang, D., & Goodman, J. 2013, PASP, 125, 306
Fornasier, S., Barucci, M. A., de Bergh, C., et al. 2009, A&A, 508, 457
Fornasier, S., Doressoundiram, A., Tozzi, G. P., et al. 2004, A&A, 421, 353
Fornasier, S., Lantz, C., Barucci, M. A., & Lazzarin, M. 2014, Icar, 233, 163
Fraser, W. C., & Brown, M. E. 2012, ApJ, 749, 33
Fraser, W. C., Brown, M. E., & Glass, F. 2015, ApJ, 804, 31
Freudling, W., Romaniello, M., Bramich, D. M., et al. 2013, A&A, 559, A96
Gomes, R., Levison, H. F., Tsiganis, K., & Morbidelli, A. 2005, Natur, 435, 466
Hardorp, J. 1980, A&A, 91, 221

Hendrix, A. R., Vilas, F., & Li, J.-Y 2016, M&PS, 51, 105
Horne, K. 1986, PASP, 98, 609
Hunter, J. D. 2007, CSE, 9, 3
Izawa, M. R. M., Applin, D. M., Norman, L., & Cloutis, E. A. 2014, Icar, 237, 159
Jones, E., Oliphant, T., Peterson, P., et al. 2001, SciPy: Open Source Scientific Tools for Python, http://www.scipy.org/
Lazzarin, M., Barucci, M. A., Boehnhardt, H., et al. 2003, AJ, 125, 1554
Levison, H. F., Morbidelli, A., Tsiganis, K., Nesvorný, D., & Gomes, R. 2011, AJ, 142, 152
Levison, H. F., Morbidelli, A., VanLaerhoven, C., et al. 2008, Icar, 196, 258
Marsset, M., Vernazza, P, Gourgeot, F, et al. 2014, A&A, 568, L7
McAdam, M. M., sunshine, J. M., Howard, K. T., et al. 2015, Icar, 245, 320
McKinnon, W. B. 2002, in Proc. Asteroids, Comets, Meteors (ACM 2002), ed. B. Warmbein (ESA SP-500; Noordwijk: ESA), 29
Merlin, F., Hromakina, T., Perna, D., et al. 2017, A&A, 604, A86
Modigliani, A., Bramich, D., Vernet, J., & Ballester, P. 2017, Very Large Telescope X-Shooter pipeline user manual (Garching, Germany: ESO), ftp://ftp.eso.org/pub/dfs/pipelines/xshooter/xshoopipeline-manual-12.16.pdf
Moffat, A. F. J. 1969, A&A, 3, 455
Mommert, M., Harris, A. W., Kiss, C., et al. 2012, A&A, 541, A93
Morbidelli, A., Levison, H. F., Tsiganis, K., & Gomes, R. 2005, Natur, 435, 462
Peixinho, N., Delsanti, A., & Doressoundiram, A. 2015, A&A, 577, A35
Raymond, S. N., & Izidoro, A. 2017, Icar, 297, 134
Rivkin, A. S. 2012, Icar, 221, 744
Rivkin, A. S., Campins, H., Emery, J. P., et al. 2015, in Asteroids IV, ed. P. Michel et al. (Tuscon, AZ: Arizona Univ. Press), 65
Rubin, A. E. 1995, Icar, 113, 156
Smoker, J., Dias, B., Mieske, S., & Kaufer, A. 2017, Very Large Telescope FORS Pipeline User Manual (Garching, Germany: ESO), ftp://ftp.eso.org/pub/dfs/pipelines/fors/fors-pipeline-manual-12.16.pdf
The Astropy Collaboration, Robitaille, T. B., Tollerud, E. J., et al. 2013, A&A, 558, A33
Tsiganis, K., Gomes, R., Morbidelli, A., & Levison, H. F. 2005, Natur, 435, 459
van der Walt, S., Colbert, S. C., & Varoquaux, G. 2011, CSE, 13, 22
Vernazza, P., Marsset, M., Beck, P., et al. 2016, AJ, 152, 54
Vernet, J., Dekker, H., D'Orico, S., et al. 2011, A&A, 536, A105
Vilas, F., & Gaffey, M. J. 1989, Sci, 246, 790
Walsh, K. J., Morbidelli, A., Raymond, S. N., O'Brien, D. P., & Mandell, A. M. 2011, Natur, 475, 206
Walsh, K. J., Morbidelli, A., Raymond, S. N., O'Brien, D. P., & Mandell, A. M. 2012, M&PS, 47, 1941